# A Novel Procedure to Determine the Effects of Debonding on Case Exposure of Solid Rocket Motors

S. Mini[1], F. Ponti[2], V. Ravaglioli[3] and D. Moro[4]

*University of Bologna, Forlì, FC, 47121, Italy*

A. Annovazzi[5]

*Avio Space Propulsion, Colleferro, Rome, 00034, Italy*

**Abstract**

Solid rocket motors are complex systems which need to withstand extreme physical conditions in terms of temperature, pressure, and high-density energy release. Therefore, specific attention should be brought to the flaws that may occur during motor manufacturing\handling phases prior to launch. An example of such flaws is debonding, usually arising at the interface between case insulation and solid grain. When debonding is significant in size, it may result in the premature case exposure to combustion chamber hot gases, and, in worst cases, it may even cause a complete motor failure. This work is intended to evaluate the impact of propellant debonding on solid rocket motor case-insulating layer, making predictions about the most unfavorable regions where the debonding could occur. Numerical simulations are performed with an in-house simulation software applied to an actual solid rocket motor stage.

KEYWORDS: solid rocket motor flaws, grain debondings, debonding effect, solid rocket motor simulation.

[1] Research Fellow, Department DIN, via Fontanelle 40, stefano.mini3@unibo.it

[2] Full Professor, Department DIN, via Fontanelle 40, fabrizio.ponti@unibo.it

[3] Senior Assistant Professor, Department DIN, via Fontanelle 40, vittorio.ravaglioli2@unibo.it

[4] Full Professor, Department DIN, via Fontanelle 40, davide.moro@unibo.it

[5] Senior Engineer, AVIO Space Propulsion Design Department, adriano.annovazzi@avio.com

# 1   Introduction

In solid rocket motors, the interface region between the case and the solid grain consists of various layers (Figure 1).

First, an insulation layer is used next to the case as a thermal coating [1] in order to protect it from the high amount of thermal power released by grain combustion [2]. Then, a thin adhesive layer, known as *liner*, bonds together the solid propellant and the thermal insulation. It is able, indeed, to establish chemical bonds between the thermal protection layer and the grain itself. The last layer, much thicker than the previous ones, is represented by solid propellant. The strength of the interface region is crucial due to the stresses and strains accumulation taking place in that region. In fact, one fundamental requirement of the interface is to withstand pressure loadings occurring during the phases before launch, from manufacturing process to transportation [3]. However, if these stresses exceed the bond strength of the interface materials, a fracture may arise through the grain which represents the weakest part between liner material and grain itself from a mechanical perspective [4,5]. Hence, the propellant may separate from the insulation layer leading to *debonding* [6].

Debonding areas are usually high-suspicion regions for two reasons. First, because the presence of debonding during combustion could cause an increase in combustion chamber pressure. Due to both debonding presence in the combustion chamber and debonding tip propagation, the debonding surface increases, contributing with additional surface area to the burning process [7], in a similar way as for grain cavities [8]. The burning surface increase leads to a pressure rise: if the pressure becomes higher than the design pressure, it may cause unsustainable mechanical deformations and even motor failure. To make matters worse, the mechanical expansion of the case could heighten debonding dilatation velocity [9]. Therefore, the higher burning surface increase implies a greater pressure rise. Second, when the burning surface reaches the debonding, the debonded area could offer a path for hot gases to prematurely attack case-insulating thermal protection layer. When thermal protections are exposed to the combustion chamber hot gases, thermal loads coming from the combustion chamber are restrained since the insulating material changes its state of matter (sublimation) absorbing most of the thermal energy close to the wall.
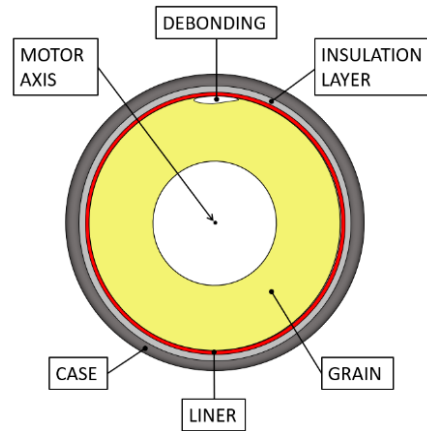
**Figure 1: Propellant debonding.**

48

49

50    Under nominal conditions, thermal protections are designed to withstand a certain amount of thermal

51    stresses for a theoretical time interval, since if they are not thick enough to absorb all the heat coming from

52    the combustion chamber, they are no longer able to insulate the case [10]. When the burning surface reaches

53    the debonding region, the thermal protection material layer is prematurely exposed to combustion chamber

54    hot gases: if all the material is depleted before the end of grain combustion, the hot gases could reach the

55    case. Also in this case, the ultimate consequence could be the launcher failure.

56    Hence, the capability to estimate the impact of debonding on solid rocket motors performance is of great

57    importance in order to guarantee that the actual performance of the launcher closely matches the nominal

58    one. Most works in the literature focus on the structural initiation\interaction of a propagating debonded

59    flaw. For instance, Wu [9,11] shows a methodology to evaluate the combustion of solid propellant in a

60    propagating debonded cavity. This model consists in linking together a 1D unsteady fluid dynamic model

61    and a 0D viscoelastic model. The main result is an effective procedure establishing a pressure limit under

62    which an existing debonding remains stable and no significant macrostructural damage appears.

63    Meanwhile, Sih [12,13] uses an iso-energy density theoretical model to predict sites of potential failure

64    initiation at the interface between liner and propellant. More in detail, local elevation of stresses and energy

65    density leading to debonding propagation are investigated. Furthermore, in line with the aim of thoroughly

66    examining debonded flaw propagation, in [14] a pure CFD model consisting of density-based Navier-

67    Stokes equations is used in order to obtain the pressure distribution within the grain-liner debonding region.

68    In addition, in [15,16] it is respectively shown how the liner properties influence the occurrence of strain

69    critical locations, i.e., where a debonding could arise and a procedure to evaluate the interface resistance

70    against debonded flaw initiation. As previously outlined, past literature on debonding impact on SRMs

71    mainly focuses on the structural causes leading to debonding initiation and propagation. Some "check"

3

72  criteria [9] are obtained with the aim of establishing if a debonding goes through an unstable propagation

73  causing chamber over-pressurization and subsequent case burn-through. However, even if debonding

74  remains stable during grain combustion, it could have a great impact on SRMs performance in terms of

75  both combustion chamber pressure increment and premature exposure of case-insulating thermal protection

76  layer, as outlined in previous paragraphs. Additionally, to the present authors' knowledge, there are no past

77  studies regarding the impact of such debonding on case thermal exposure.

78  The aim of this work is the evaluation of the most critical zones in terms of case insulation exposure, by

79  proposing a procedure to reconstruct the SRM case exposure map of a generic-shaped debonding. Knowing

80  the most dangerous debonding positions on SRM case is fundamental at the time of the structural integrity

81  inspection of a solid rocket. In general, the occurrence of debonding is checked through radiography as a

82  non-destructive diagnostic tool for measuring debonding surface extension [17,18]. More in detail, an

83  ordinary x-ray imaging system[19–21] is used to inspect propellant bulk and case thermal protection with

84  a flaw size accuracy of about 0.5 mm [22]. Inspection tests are performed on both the overall motor and/or

85  at specific regions. Knowing the most critical case exposure regions, it is possible to drive the radiography

86  planning in the direction of a high-resolution local inspection next to critical areas, and a low-resolution

87  radiography in the remaining zones. Through the above-mentioned approach it is possible to devote most

88  time and effort to debonding in critical regions only, obtaining a more effective and optimized usage of the

89  x-ray technique in order to identify debond flaws in such regions. Furthermore, the method introduced in

90  the present work could be used to determine the effect on case exposure caused by debonding detected

91  through radiography observations. If the early exposure of the thermal protection material due to the

92  debonding region is considered unacceptable, the solid rocket stage could probably undergo specific

93  attempts of be repaired before final firing. Moreover, it is important to emphasize that the present study is

94  meant to investigate the debonding impact on SRMs integrity rather than debonding structural stability as

95  in previous literature. The proposed procedure allows for the evaluation of the risk linked to a generic

96  debonding by considering its effect in terms of case thermal protection exposure anticipation with respect

97  to the nominal condition without debonding, where the nominal case exposure condition is obtained with

98  ROBOOST [23,24], namely ROcket BOOst Simulation Tool internal ballistics software. That software has

99  been previously validated on an actual SRM, specifically, ZEFIRO 9, in [8]. Hence, ROBOOST software

100 tool is considered a reliable instrument to confirm the adequacy of the novel procedure aimed to determine

101 debonding influence on thermal protections exposure.

102

4

## 2   Code Overview

The first step of the proposed procedure consists in determining a map of the thermal protection exposure, and a map of the angle of arrival of the combustion surface on the thermal protection layer. Both maps are used to determine the effects of a debonding in terms of additional exposure of the thermal protection to the hot gases that are present inside the combustion chamber and are evaluated using ROBOOST software. One of the outputs that ROBOOST can provide is, in fact, the 3D representation of the burning surface discretized with a triangular mesh: tracking the burning surface vertices that lay on the SRM case at each simulation iteration, it is possible to determine when the corresponding case position begins to be exposed to the combustion chamber hot gases, and evaluate the orientation (i.e., the direction of incidence) of the burning surface motion when approaching the thermal protection surface. Identification of the burning surface vertices laying on the case is possible simply looking at the points that belong to the free boundary triangular facets (i.e., mesh edges) of the mesh itself.

A mesh edge in the triangulation is on the free boundary if it is referenced by only one triangle of the mesh describing the combustion surface, implying that the set of free boundary vertices coincides with the set of outer edges of the 3D triangulation. Figure 3 shows at different ROBOOST iterations, namely $n_k$ and $n_h$ with $h > k$, mesh free boundary points moving from the positions marked in blue to the new positions represented by green dots. At a specified iteration, each free boundary mesh vertex is uniquely linked to both a specific point on the case surface and an iteration number. Since it is possible to evaluate the corresponding web consumption (i.e., the thickness of burned propellant) at each iteration, each case position can be associated with a single burning surface regression iteration, and thus, with a single value of the web consumption. That value represents the web position where case exposure to the combustion chamber hot gases begins.

As already mentioned, identifying mesh edges on the free boundary is possible because each edge is referenced by a unique triangle of the mesh describing the combustion surface. The evaluation of the normal vector to each of the triangles containing the mesh edges on the free boundary indicates the direction of arrival of the combustion surface on the thermal protection. The inclination of the direction of arrival with respect to the thermal protection surface describes the angle of arrival $\delta$ (Figure 2) of the combustion process on the thermal protection surface. The angle $\delta$ can range from 0° (when the burning surface is orthogonal to the local thermal protection surface, thus moving tangentially to it) to 90° (when the combustion surface reaches the thermal protection layer moving along a orthogonal direction to it). As it will be shown in the following sections, the evaluation of the angle $\delta$ is important in order to determine the effect of debonding thickness, i.e., the extension along an orthogonal direction with respect to the thermal protection surface.
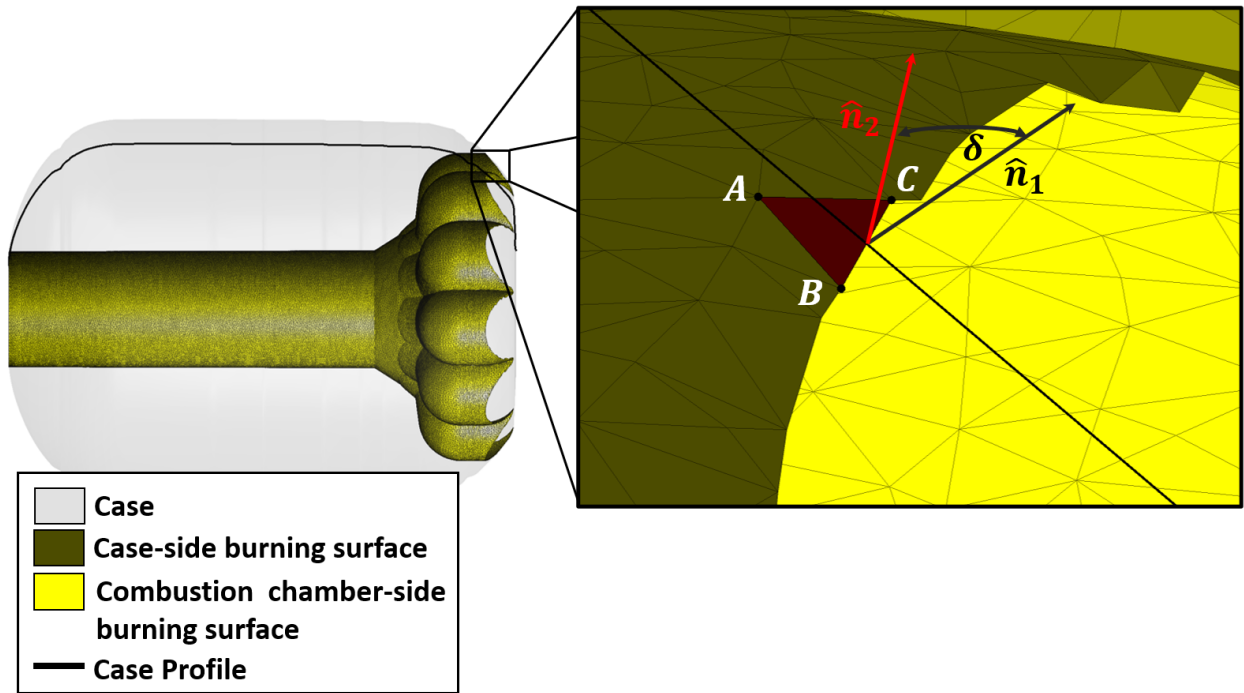
5

136



**Figure 2: combustion surface-to-thermal protection arrival angle**
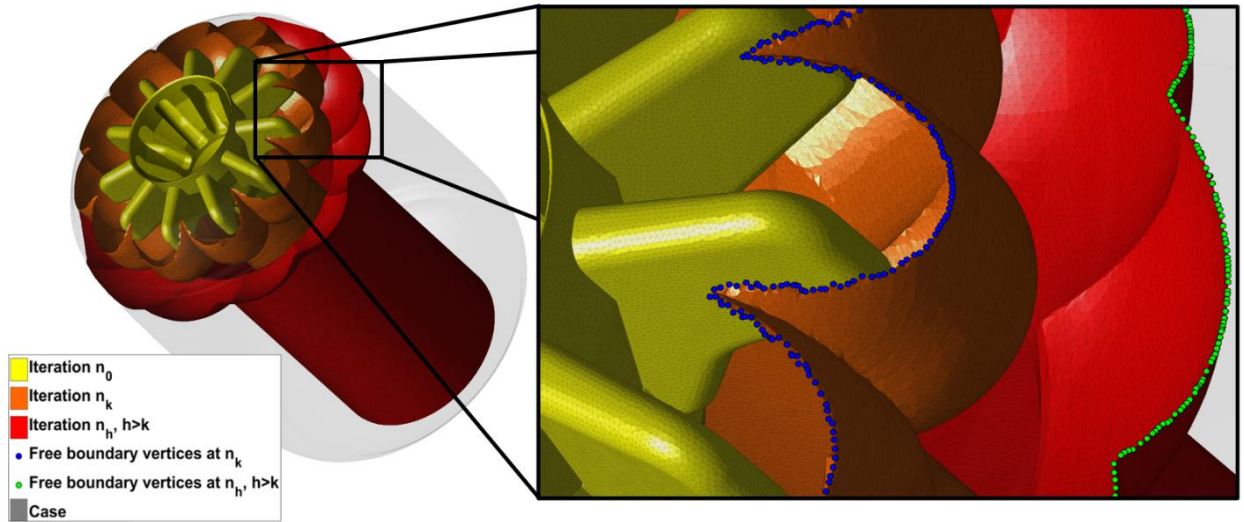
137

138



**Figure 3: Mesh free boundary vertices.**

139

140

141 Once the web consumption coordinate is obtained, it can be used to express thermal protection exposure

142 based on the following assumptions: web consumption value is equal to 0 (at iteration $n_0$) for all the free

143     boundary vertices of the initial mesh; the actual value can be obtained as the distance covered by the burning

144     surface to reach the actual positions; its maximum value is evaluated when the last portion of burning

145     surface reaches the case. Consequently, a thermal protection exposure parameter can be established as the

146     difference between the maximum web consumption and the local value associated to each case surface

147     point. The identified parameter has the same units as the web consumption, and it is named from now on

148     web exposure. Applying the evaluation to each point on the case surface, the outcome is a map of web

149     exposure values defined over the whole thermal protection describing its gradual uncovering: high web

150     exposure values correspond to case regions where the propellant is burned earlier with respect to case zones

151     with lower web exposure values. More in detail, zero web exposure values are linked to those case surface

152     zones which are exposed to combustion chamber hot gases at the burn-out phase; while maximum web

153     exposure is associated to case regions which are exposed to hot gasses at the beginning of the combustion

154     process. Hence, with the above-mentioned definitions, web exposure maps do not depend on the burning

155     rate at a specific time instant anymore, but rather they are suitable for general values of burning rate.

156     The presence of a debonding on the propellant-thermal protections interface creates a variation of the web

157     exposure, since it causes a quicker spreading of the flame along the flaw of the internal surface and within

158     its volume. It can be easily stated that the web exposure variation generated by a debonding depends on its

159     location and dimensions. The aim of the procedure described in the following paragraphs is to estimate

160     these effects.

161     *2.1   Debonding positioning effect*

162     The most suitable parameter to describe the influence of a flaw position is the gradient of the web exposure

163     which is directly linked to the local variation of the web exposure and corresponds to the rate of change of

164     the web exposure that is generated by the presence of an infinitesimal debonding located in each position

165     of the case. It must be emphasized that the gradient value does not depend on debonding shape, however,

166     it is used to show the most critical debonding in terms of its position on the case.

167     The representation of the web exposure map and its gradient is done using the reference frame represented

168     in red in Figure 4. It consists of three perpendicular unit vectors: $e_{x_c}$ identifies the curvilinear coordinate

169     along the case profile $(x_c)$, $e_{az}$ is the azimuthal coordinate unit vector along the circumferential direction

170     $(x_{az})$ around the motor axis $e_z$, $e_{x_n}$ corresponds to the perpendicular direction to the plane of the case

171     profile $(x_n)$, while the center $(O')$ of the local reference frame is taken on the case surface. The zero level

172     of the curvilinear coordinate $x_c$ is assumed at the intersection between the black case profile and the vertical

173     axis (point $Q$ in Figure 5), i.e., at the beginning of the case close to the igniter side. Hence, $x_c$ increases

174     moving along the case from the igniter side to the nozzle one. Since exposure maps are computed on the

7

175 case surface, the local reference frame $O'x_cx_{az}x_n$ establishes two coordinates needed for the graphical

176 representation of the maps. Such quantities are $x_c$ (curvilinear coordinate) and $x_{az}$ (azimuthal coordinate).
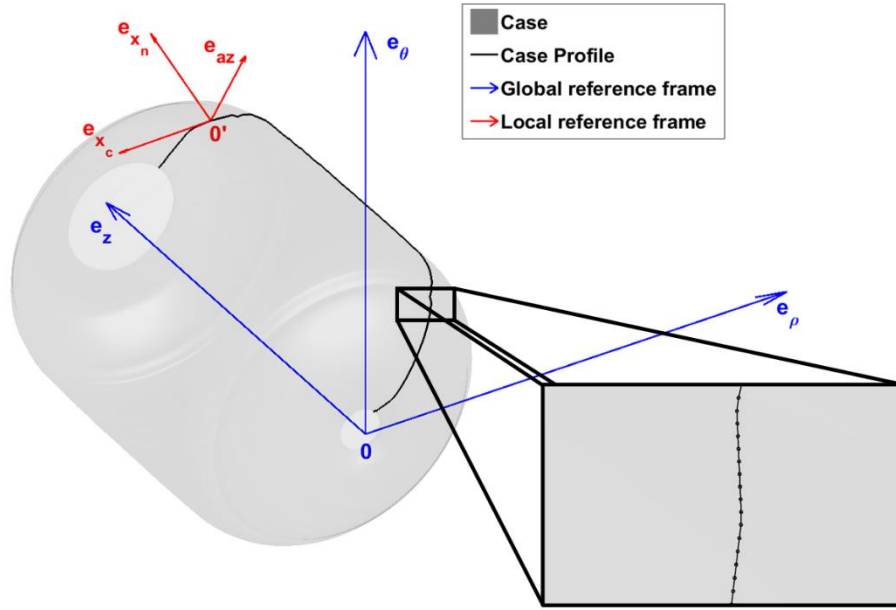
177



**Figure 4: Reference frames.**

178

179

180 As already mentioned, these coordinates are used to display the web exposure map and to compute the case

181 web exposure gradient.

182 Based on the provided definitions, the gradient of the web exposure map $\phi$ is computed using Eq. (1).

183

$$\nabla\phi = h_{x_c}\frac{\partial\phi}{\partial x_c}\vec{e}_{x_c} + h_{az}\frac{\partial\phi}{\partial x_{az,\theta}}\vec{e}_{az}$$

$$h_{x_c} = 1$$

(1)

$$h_{az} = \frac{1}{\left(x_c - x_{c_{o'}}\right)\sqrt{\dfrac{\beta^2}{\beta^2+\alpha^2}} + \rho_{O'}}$$

184

185 where $h_{x_c}$ and $h_{az}$ are the *Lamè coefficients* respectively referred to the curvilinear coordinate and the

186 azimuthal coordinate; $\rho_{O'}$ is the local reference frame center radial position (Figure 5) expressed in the

8

187  global cylindrical reference frame; $x_{c_0}$, is the curvilinear coordinate value up to the center of the local

188  reference frame. The detailed procedure to obtain the Lamè coefficients is shown in Appendix A. The case

189  profile is discretized into a certain number of small linear segments along the curvilinear coordinate

190  (segment $AO'$ in Figure 5). That linear approximation guarantees a simpler form of the *Lamè coefficients*

191  regarding the gradient expression without loss of accuracy. In fact, simply by increasing the number of

192  linear discretization segments, a more refined gradient map that follows the case profile curvature more

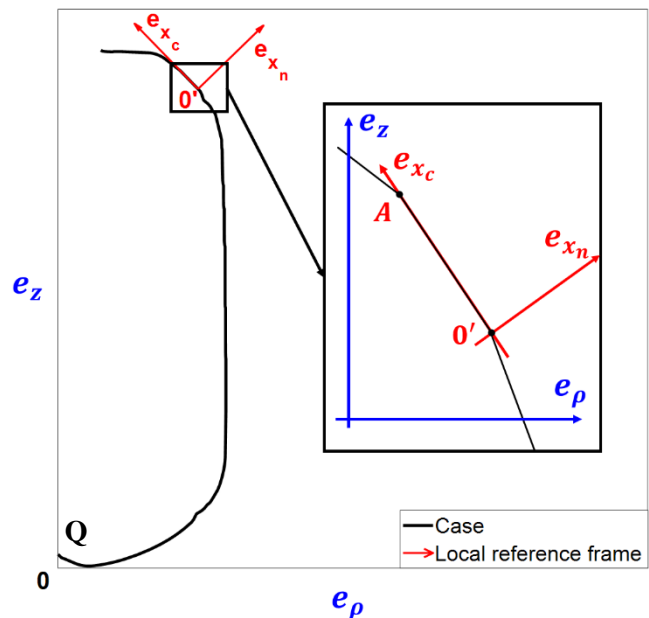193  consistently is obtained.

194

195



**Figure 5: Reference frame for gradient computation.**

196

197

198  Figure 5 highlights the applied discretization process. It can be noticed that the blue reference frame in the

199  figure is the same global reference frame of Figure 4 but it is expressed with respect to the motor axis; Eq.

200  (1) is computed for each discretization segment of the case (segment $AO'$ in Figure 5); $\alpha$ and $\beta$ are defined

201  by Eq. (2), representing the straight line passing through the two segment vertices (like $A$ and $O'$).

202

$$\alpha\rho + \beta z + \gamma = 0 \qquad (2)$$

203

204  As pointed out before, the local reference frame is sequentially moved on each segment of the case in order

205  to evaluate segment-by-segment the gradient value of the case-insulating exposure map. Equation (3) shows

9

206   the formula linking $x_{az}$ and $x_{az,\theta}$: the gradient was estimated by considering the azimuthal coordinate

207   expressed in angle units ($x_{az,\theta}$).

208

$$x_{az} = \rho \cdot x_{az,\theta} \tag{3}$$

209

210   From here on, $x_{az}$ will be named arc azimuthal coordinate, whereas $x_{az,\theta}$ will be identified as angular

211   azimuthal coordinate. Finally, $\frac{\partial \phi}{\partial x_c}$ and $\frac{\partial \phi}{\partial x_{az,\theta}}$ are approximated using a second order centered scheme

212   respectively along the curvilinear coordinate and the azimuthal direction.

213   *2.2   Debonding dimension effects*

214   The gradient map of web exposure evaluated on the thermal protection layer can highlight the most

215   dangerous positions, independently of the flaw dimension. The effect of debonding extension along the

216   case curvilinear coordinate $x_c$ and azimuthal coordinate $x_{az}$ is now investigated through a dedicated

217   procedure using the same concept already introduced when considering the local gradient.

218   First, size and geometry of the debonding along $x_c$ and $x_{az}$ are chosen (in Figure 6 the displayed debonding

219   has a square-shaped geometry with dimensions $L_{x_c}$ and $L_{az}$). Then, the debonding is positioned at different

220   points on the case exposure map (in Figure 6 case exposure map is represented with a black curve bounding

221   the debonding). The new map, namely *exposure increase map*, is computed by associating at each point

222   (representing the debonding center, like point P in Figure 6) the difference between the maximum and the

223   minimum web exposure among the exposure values restrained by the debonding geometry on the web

224   exposure map. The exposure increase map is then associated to the maximum effect a debonding positioned

225   at each point on the case surface can cause on the thermal protection exposure time.
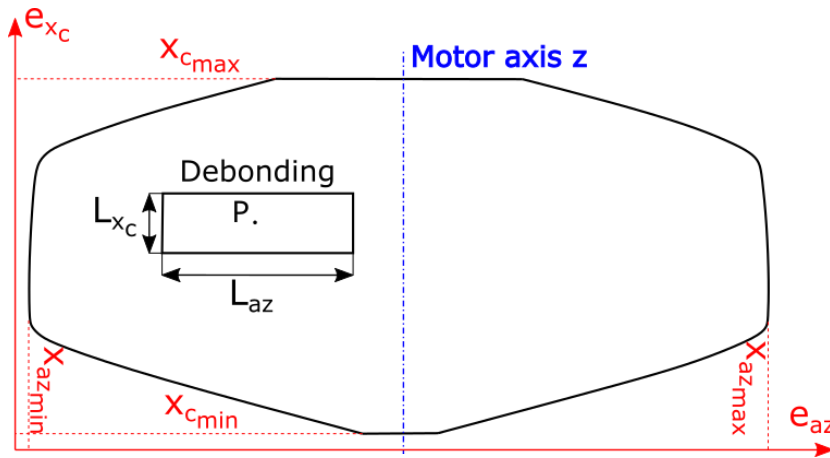


Figure 6: Debonding influence map generation.

226

227

228 The debonding size along the direction $e_{x_n}$, i.e. the debonding thickness, usually has a negligible effect in

229 terms of anticipating the thermal protection case exposure with respect to the nominal value. Indeed, in

230 actual debondings, the thickness is an order of magnitude lower than the other two dimensions, namely $L_{x_c}$

231 and $L_{az}$. For the sake of completeness and to address also those cases where thickness is not negligible, its

232 effect and value is discussed in the next paragraphs. The maximum exposure advance due to the debonding

233 thickness occurs when the burning surface moving toward the debonding remains parallel to the case. In a

234 general situation the effect of thickness is associated with both the extension $L_{x_n}$ of the debonding in the

235 direction $e_{x_n}$, and the angle $\delta$ between the combustion surface regression direction and the thermal

236 protection surface, as expressed by Equation (4):

237

$$\Delta exp_{th} = L_{x_n} \cdot sin(\delta) \tag{4}$$

238

239 Equation (4) clearly shows that the effect of thickness is directly proportional to the thickness value $L_{x_n}$,

240 and depends on $\delta$, with the largest influence associated with its 90° value. Exposure advance evaluated

241 through Equation (4) indicates how much the minimum web exposure of the debonding footprint on the

242 thermal protection is further anticipated due to its thickness. Based on these considerations, the exposure

243 increase map should be evaluated as:

244

$$\Delta exp = max(web\ exp)_{deb} - min(web\ exp - \Delta exp_{th})_{deb} \tag{5}$$

245

246 It is of fundamental importance to highlight that this map (Figure 6) does not only allow for the investigation

247 of debonding extended in one direction ($e_{x_c}$ or $e_{az}$). As a matter of fact, such method also offers the

248 possibility to deal with flaws characterized by generic aspect ratio values, where the aspect ratio is intended

249 as the ratio between $L_{x_c}$ and $L_{az}$. Even more, generic-shaped flaws can be included as well. In fact, in order

250 to generate the debonding position influence map, it is sufficient to superimpose the debonding generic

251 shape on the case exposure map and evaluating, as already mentioned before, the maximum difference

252 among the exposure values bounded by the debonding itself.

253 The above-mentioned procedure has been validated with respect to ROBOOST software by comparing the

254 obtained results for a series of appropriately designed flaws. Their location has been conveniently chosen

255 in the direction of investigating both the most critical positions on the case and the impact of the debonding

256 direction of elongation.

## 3 Results and discussion

257

258 The map generation method explained in the previous chapter has been applied to the third stage of Vega
259 launcher, namely, ZEFIRO 9 (Z9).
260 Vega is designed to launch small payloads: up to 1500 kg satellites for scientific and Earth observation
261 missions in low Earth orbits. It consists of four stages: three of them are solid propellant based, the fourth
262 is a liquid propellant engine. Z9 is 3.5 m tall, has a diameter of slightly less than 2 m, weighs 11,500 kg,
263 and burns 10,500 kg of HTPB based composite propellant. Regarding the propellant geometry
264 configuration, it has been designed with a circular section in the fore and central parts, and with a finocyl
265 shaped configuration in the rear part near the nozzle inlet (Figure 7).

266
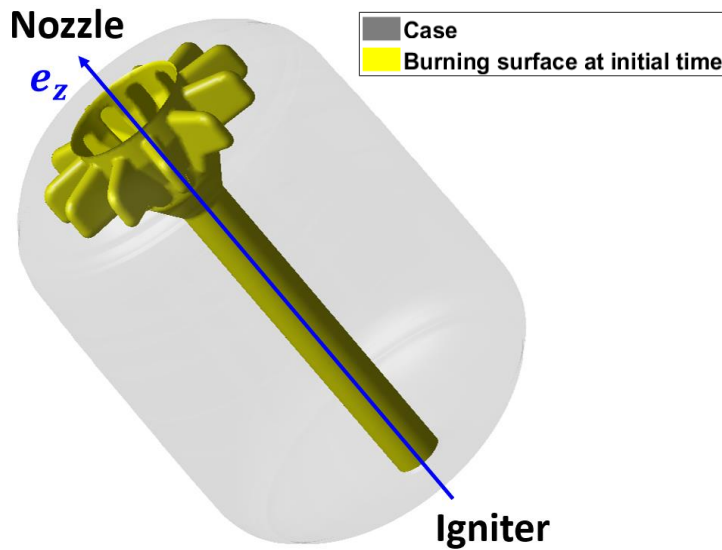


**Figure 7: ZEFIRO 9 central bore.**

267

268

269 Figure 8 shows the web exposure map and its gradient in the different direction for the Z9 motor. In
270 particular Figure 8a shows the case-insulating thermal protection exposure map. The web exposure has
271 been normalized by dividing all values by its maximum value. The same procedure has been performed for
272 both the curvilinear coordinate $x_c$ and the azimuthal coordinate $x_{az}$, respectively dividing them with respect
273 to the two maximum values $x_{c_{max}}$ and $x_{az_{max}}$.

274

12

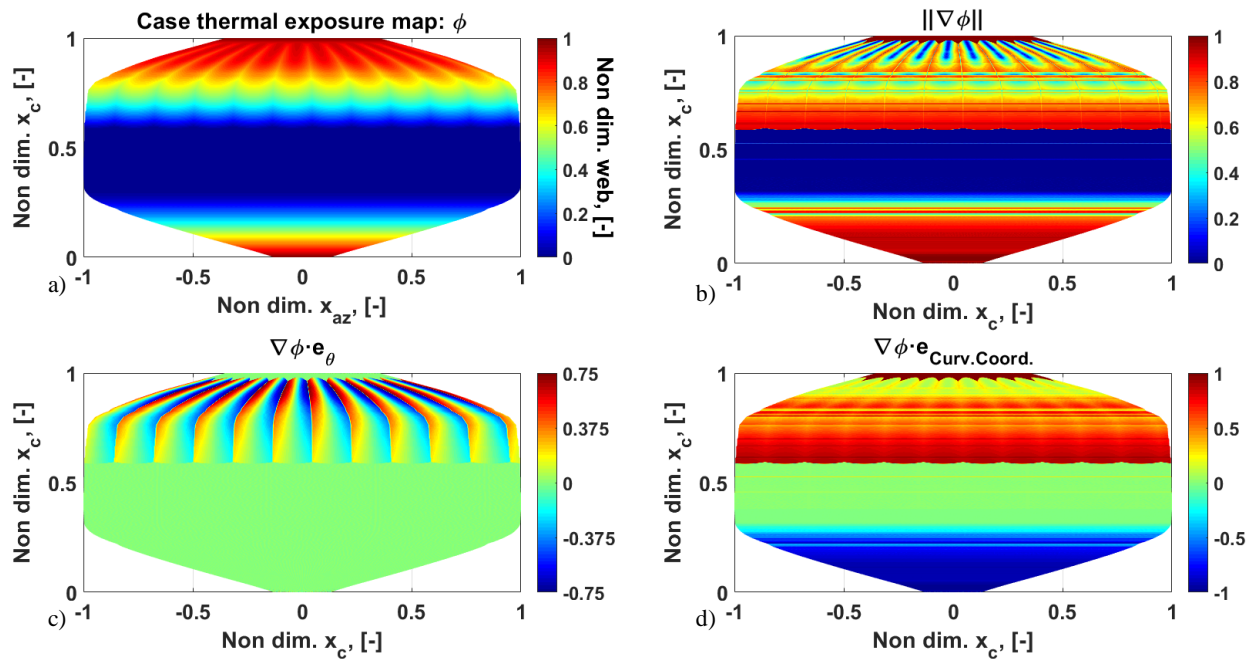**Figure 8: Maps linked to case exposure and case exposure gradient.**

The above-mentioned map shows the maximum exposure close to the curvilinear coordinate level corresponding to the fynocil region of the burning surface (Figure 7). Indeed, the local distance between each lobe of the fynocil configuration and the case is lower than the distance referred to the burning surface cylindrical region. Thus, it is evident that the case region with the fynocil shape is exposed to combustion chamber hot gases earlier than the other regions. However, there are other regions of the SRM which present such an early exposure. These zones are the end of the cylindrical shape and the end of the fynocil respectively in proximity of the igniter and of the nozzle. In fact, the burning surface recedes along the case meaning that, during its outward advancement in radial direction with respect to the motor axis, the propellant is gradually depleted causing the local uncovering of the case thermal protection layer. Figure 8b displays the gradient norm regarding the exposure influence of debonding with an aspect ratio, computed by dividing its azimuthal coordinate and curvilinear coordinate elongation, is close to 1. Highly critical locations are depicted with red color, nearly zero gradient zones with blue color.

Figure 8c and d are respectively linked to the projection of case exposure map gradient along the azimuthal coordinate direction ($e_{az}$) and the curvilinear coordinate direction ($e_{x_c}$). In Figure 8c the green regions correspond to a zero-value gradient implying that a low impact on thermal exposure occurs for debonding mainly elongated along the azimuthal coordinate. The above-mentioned statement can be explained in accordance with the burning surface motion toward the case, indicating that the burning surface reaches the

13

294   case remaining parallel to it. The same considerations are valid for green regions in Figure 8d, where the
295   gradient trend is linked to debonding mainly elongated along the curvilinear coordinate direction. On the
296   other hand, regions with high gradient values (dark red and dark blue regions) regard case portions where
297   any debonding could significatively impact the thermal protection exposition in terms of web exposure
298   anticipation.
299   The observation of these maps allows determining the most critical regions where diagnostic procedures
300   should focus to identify flaws and also highlight the most dangerous direction along which the debonding
301   extension should be checked.
302   The following step is to evaluate the effect caused by the dimension of the flaws following the procedure
303   previously described. According to the local reference frame directions (red reference frame in Figure 6),
304   three sets of debonding are evaluated. The first set is characterized by the main elongation along the
305   azimuthal coordinate, while the second set is linked to the curvilinear coordinate elongation. The above-
306   mentioned debonding shapes are characterized by a large elongation along a specified main direction linked
307   to curvilinear or azimuthal coordinate. Since the procedure developed in this work allows the analysis of a
308   generic debonding shape regardless of the direction of the main extension, a third debonding with the same
309   magnitude along the two main directions, i.e., curvilinear, and azimuthal, has been investigated.

310   *3.1   First set of debonding*

311   The length of the main dimension of the flaw has been chosen equal to $207\ mm$. The reason for this choice
312   is associated with the evaluation of the minimum distance between two zero level regions containing the
313   maximum absolute peak (positive or negative) in Figure 8c. This extension of the flaw is in fact capable of
314   generating the highest thermal protection exposure increment in the azimuthal direction and, for this reason,
315   it is particularly interesting.
316   Based on this choice, the dimensions of the first set of debonding are as follows: $L_{az} = 207\ mm$, $L_{x_c} =$
317   $10\ mm$ and $L_{x_n} = 5\ mm$. $L_{x_c}$ and $L_{x_n}$ have been set respectively to $10\ mm$ and $5\ mm$ with the aim of
318   obtaining a debonding mainly extended along $e_{az}$. Another debonding (debonding 1a in Figure 9) was
319   considered with the same position, curvilinear and azimuthal extension of debonding 1 (Figure 9) but with
320   thickness $L_{x_n}$ equal to 15 mm in order to investigate the web exposure induced by debonding thickness
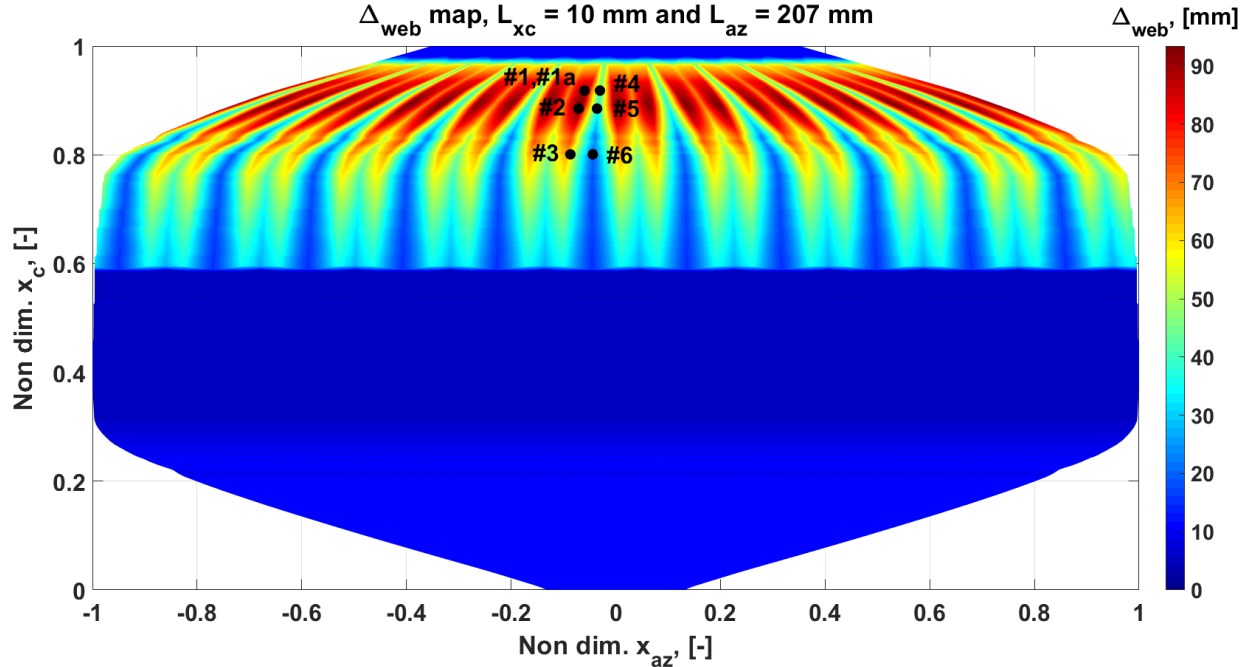321   increment.
322

14

**Figure 9: Debonding influence map regarding debonding elongation along $e_{az}$.**

The exposure increase map shown in Figure 9 is obtained following the procedure outlined in the previous section for the first set of flaws. Each point on the map represents the exposure increase that would be generated by a debonding characterized by the pre-defined geometry and centered on that point, with respect to the nominal motor. Eleven green-to-red colored regions are shown in the higher portion of Figure 9: each region corresponds to an evenly spaced lobe associated with the propellant finocyl configuration of Z9. Each of the identified regions contains two light red strips that are characterized by a dark red spot. The location of that spot corresponds to the maximum exposure increase ($76\ mm$) and coincides with the maximum gradient position in Figure 8c.

In order to validate the obtained results, seven debonding positions (black dots in Figure 9, marked from 1 to 6) have been chosen, located at 3 levels of $x_c$ and 2 levels of $x_{az,\theta}$ ($x_{az,\theta} = -16.55°$ and $x_{az,\theta} = -8°$): in particular debonding $1, 1a, 2, 3$ belong to level $x_{az,\theta} = -16.55°$, while debonding $4, 5, 6$ belong to level $x_{az,\theta} = -8°$.

Each position is subsequently implemented inside the tool ROBOOST to perform a complete regression simulation, obtaining the corresponding 3D evolution of the burning surface. After running the simulations, the web exposure map is determined following the approach already explained in the previous paragraphs and schematized also in Figure 3. Web exposure maps with and without debonding are then compared, and the differences are shown in Figure 10. The results obtained for the different positions investigated are

15

342    reported in the same figure for the sake of compactness. Each result is presented within a box, while in the

343    remaining thermal protection surface there are not any effects and the exposure difference is equal to 0

344    (blue background). Each of the boxes is connected to a white dot, marking the real position where the

345    content of the box should be located, and contains the exposure increase generated by each debonding

346    position together with the corresponding color scale ranging from 0 to the maximum value observed. Within

347    each box, the blue regions are associated with an exposure increase that is equal to 0, while the surfaces

348    affected by the debonding are marked by other colors, where dark red is associated with the highest value.

349    The shape of the regions affected by the debonding is significatively different as it can be seen comparing

350    the content of the boxes. The debonding set at $x_{az,\theta} = -16.55°$ (debonding 1, 1a, 2 and 3) presents only

351    one affected region for each debonding, while debonding set at $x_{az,\theta} = -8°$ (debonding 4, 5 and 6) is

352    characterized by two (almost symmetrical) affected regions. This difference is due to the fact that for

353    positions 1, 1a, 2 and 3 the combustion surface reaches the debonded surface on one of the two sides of the

354    flaw (as shown in Figure 11a), while for positions 4, 5 and 6 the combustion surface intersects the debonded

355    surface at its midpoint and, from that condition on, two combustion-regression fronts simultaneously spread

356    from the above-mentioned midpoint towards debonding side points (Figure 11b). Furthermore, since the

357    thickness of deboding 1a is larger then the thickenss of debonding 1, the burning surface reaches debonding

358    1a first, implying a higher web exposure increment (96 mm) compared to debonding 1(87 mm).
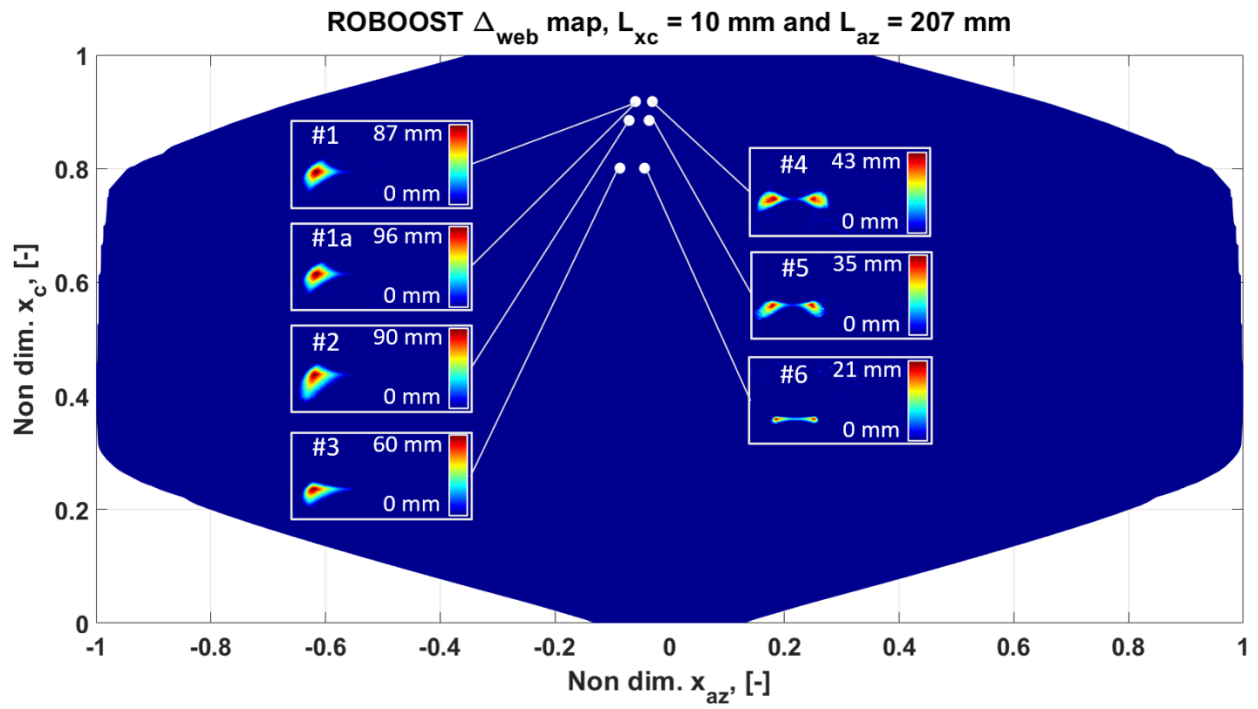
359

**Figure 10: ROBOOST simulations regarding debonding elongated along azimuthal direction.**
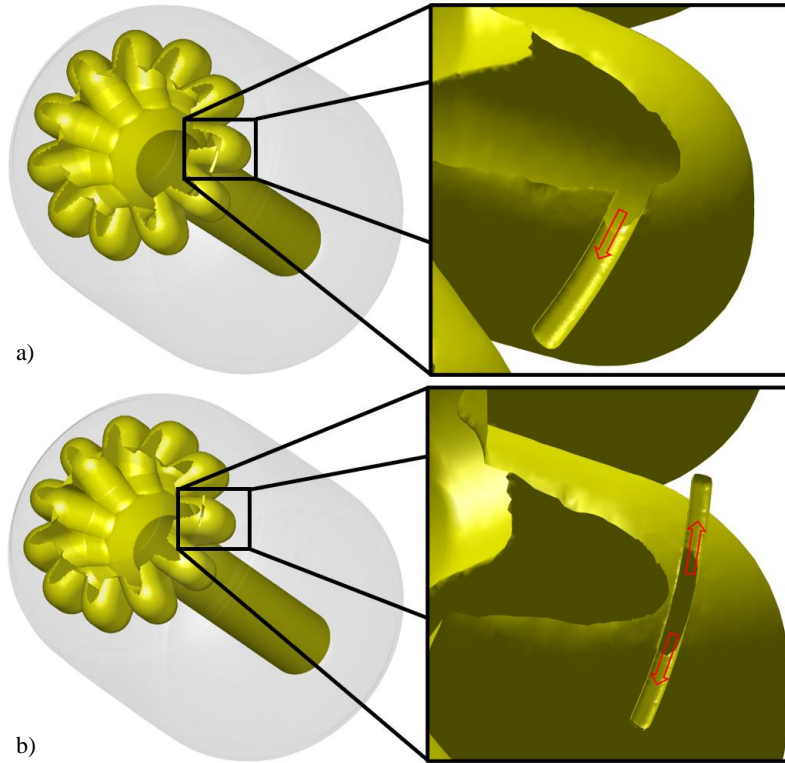
360
361

**Figure 11: ROBOOST regression of debonding 1 (a) and 4 (b).**

362

363

364

365     The maximum exposure increase obtained for each simulation can now be compared with the value

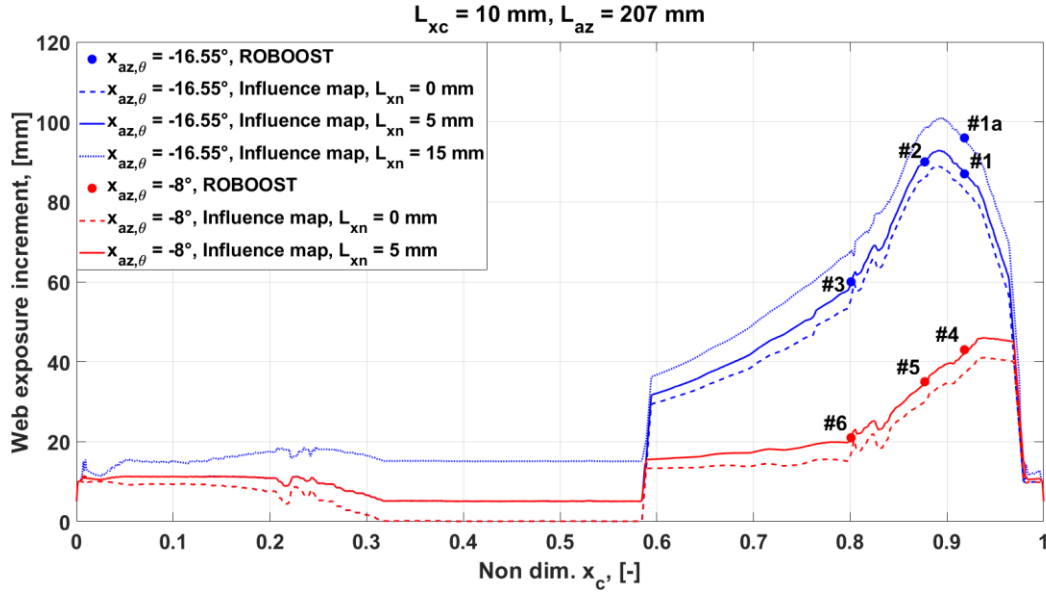366     determined with the geometrical approach developed in this work, as shown in Figure 12.

367

**Figure 12: Comparison between ROBOOST results and debonding influence map with debonding main elongation along $e_{az}$**

Each curve is obtained by representing the exposure increase map (Figure 9) at fixed values of the angular azimuthal coordinate ($x_{az,\theta} = -16.55°$ and $x_{az,\theta} = -8°$ for simulations 1, 1a, 2, 3 and 4, 5, 6 respectively) and considering the effect of different debonding thickness values ($L_{x_n} = 5\ mm$ for debondings 1 to 6 and $L_{x_n} = 15\ mm$ for debonding 1a). Moreover, the exposure increases map trends at $L_{x_n} = 0\ mm$ were included to cover the instance of earlier exposure of a region of the thermal protection case surface due to hot gas penetration between the thermal protection layer and the grain. In fact, combustion chamber hot gas could produce a crack progressively igniting the grain surface corresponding to the flaw zone. It must be highlighted that such mechanism is different from the one linked to a debonding with a non-zero thickness value. The former is characterized by the earlier exposure of the thermal protection layer caused by a nearly zero thickness flaw produced by hot gases, while the latter origins from an already present debonding with a finite thickness, leading to a more significant web exposure increment (Figure 12)

Figure 12 shows a good agreement between the estimation of the debonding effects evaluated through the methodology developed in this paper and the exposure increase determined for the 7 simulations run with ROBOOST. The maximum difference is equal to 0.78 mm, corresponding to a percentual error of 1.8 %.

*3.2   Second set of debonding*

The same analysis has been performed also on the second set of debonding, characterized by a major elongation along the curvilinear coordinate. The same debonding dimensions discussed before are inverted

387 so that $L_{x_c} = 207\ mm$ and $L_{az} = 10\ mm$, while thickness $L_{x_n} = 5\ mm$ is unchanged. The exposure

388 increase map obtained following the procedure previously introduced is shown in Figure 13.

389 Observation of Figure 13 marks out higher exposure increase values up to nearly 201 mm with respect to

390 93 mm of the maximum exposure linked to Figure 9, meaning that a debonding with $L_{x_c} \gg L_{az}$ can be

391 more critical than a debonding with $L_{x_c} \ll L_{az}$ in the case regions of maximum exposure.

392 Similarly to what was done for the previous set of debonding, also this set was validated through some

393 simulations run on ROBOOST (marked by the black dots in Figure 13 and the white dots in Figure 14), in

394 order to obtain the corresponding exposure increase values. The results of these simulations are represented

395 for the sake of compactness in the same Figure 14

396 Figure 15 shows the comparison between the evaluations coming from the procedure proposed in this paper

397 and the simulations performed with ROBOOST. The maximum difference is equal to 1 mm, corresponding
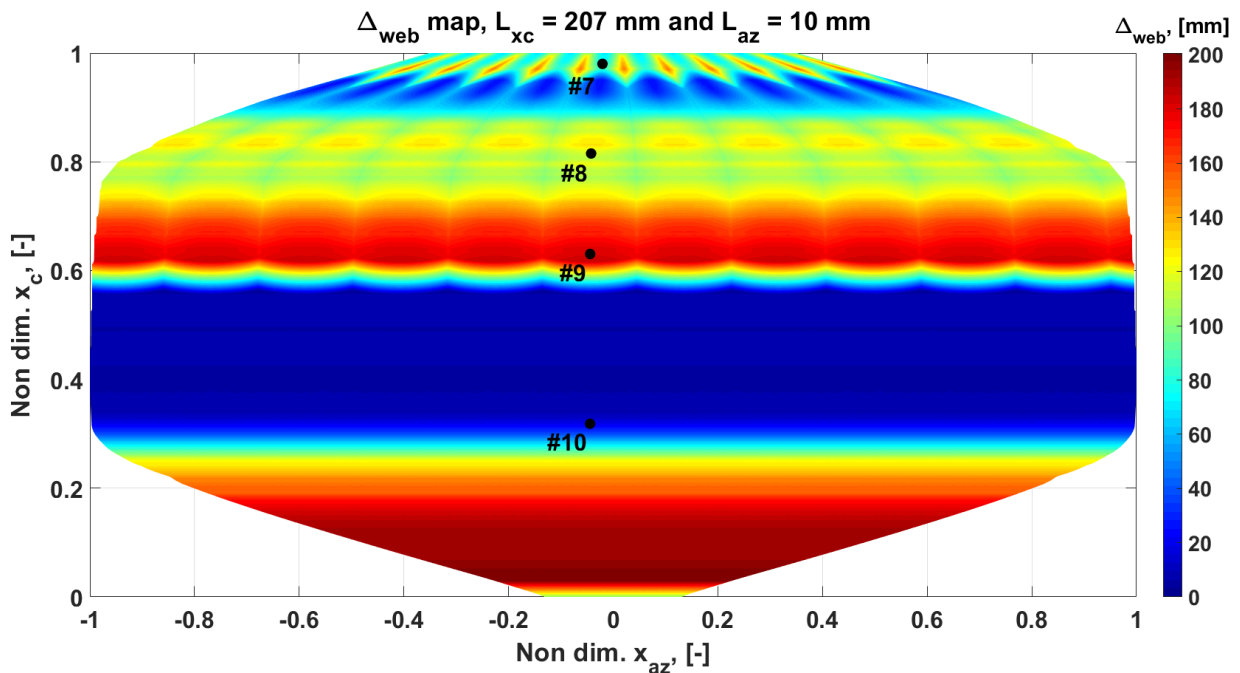
398 to a percentual error of 0.8 %.

399



Figure 13: Influence map determined for debonding mainly developed along $e_{x_c}$
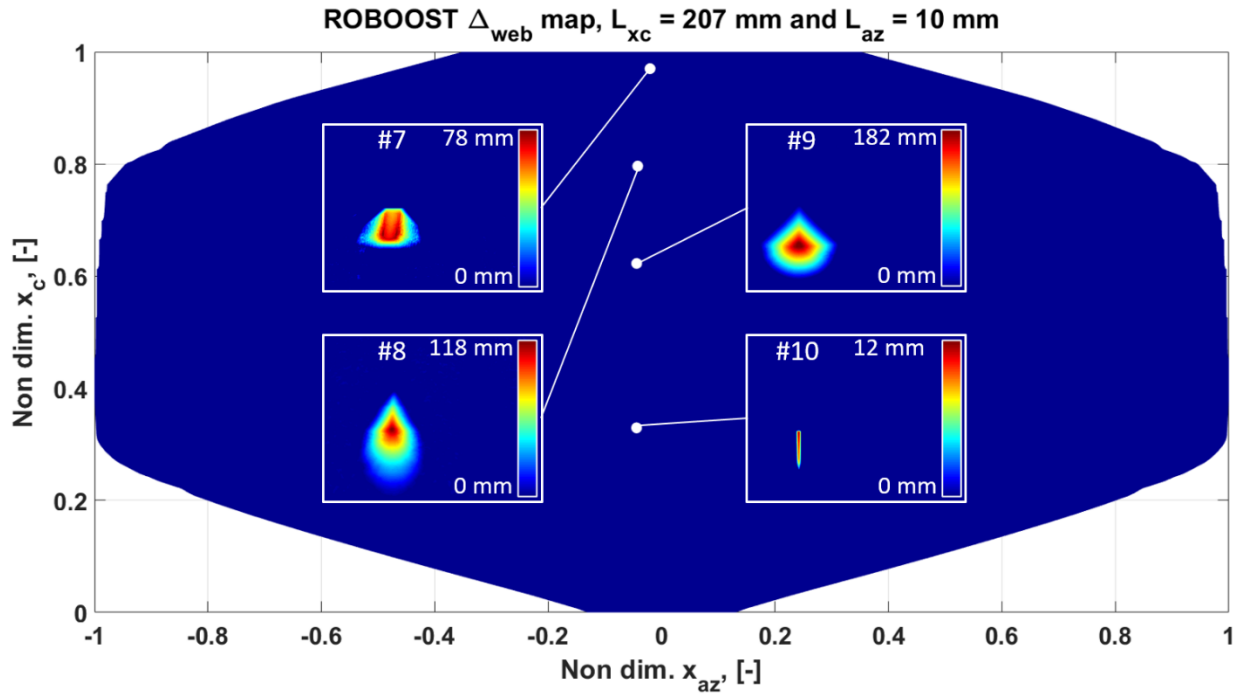
400

401

**Figure 14: ROBOOST simulations regarding debonding developed along curvilinear coordinate direction.**
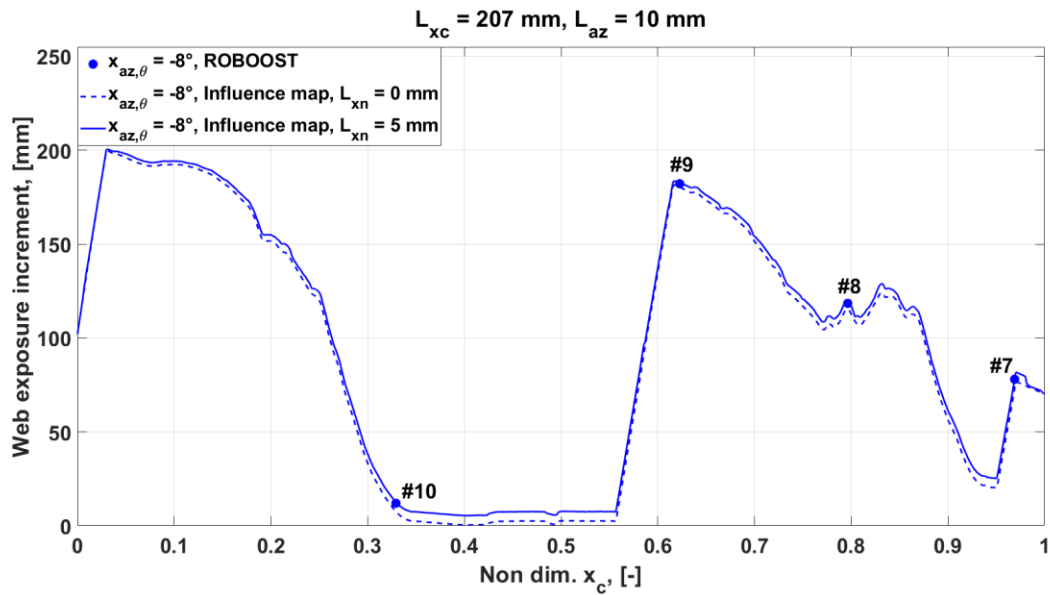
402

403



**Figure 15: Comparison between ROBOOST results and debonding influence map with debonding main elongation along $e_{x_c}$**

404

405

406    Previous debondings are respectively identified by the main elongation along azimuthal direction or along
407    the curvilinear coordinate. However, the procedure outlined in the present work is also valid for debondings
408    extended along both curvilinear and azimuthal directions. According to the above-mentioned statement, a
409    debonding with the following dimensions was chosen: $L_{x_c} = 207\ mm$, $L_{az} = 207\ mm$ and $L_{x_n} = 5\ mm$.
410    First, the corresponding debonding influence map was determined with the method used to compute
411    previous contour plots (Figure 9, Figure 13). Then, the maximum web exposure increment of the debonding
412    was identified at $x_{az,\theta} = -18.25°$ and $x_c/x_{c_{max}} = 0.6$. Finally, ROBOOST simulation was performed
413    evaluating the impact of such debonding in the maximum web exposure increment position on the thermal
414    protection case, with an exposition of 207 mm. Figure 16 shows a good agreement between the result
415    obtained through ROBOOST and the debonding influence map prediction. The difference is equal to 1.1
416    mm, corresponding to a percentual error of 0.5 %.
417
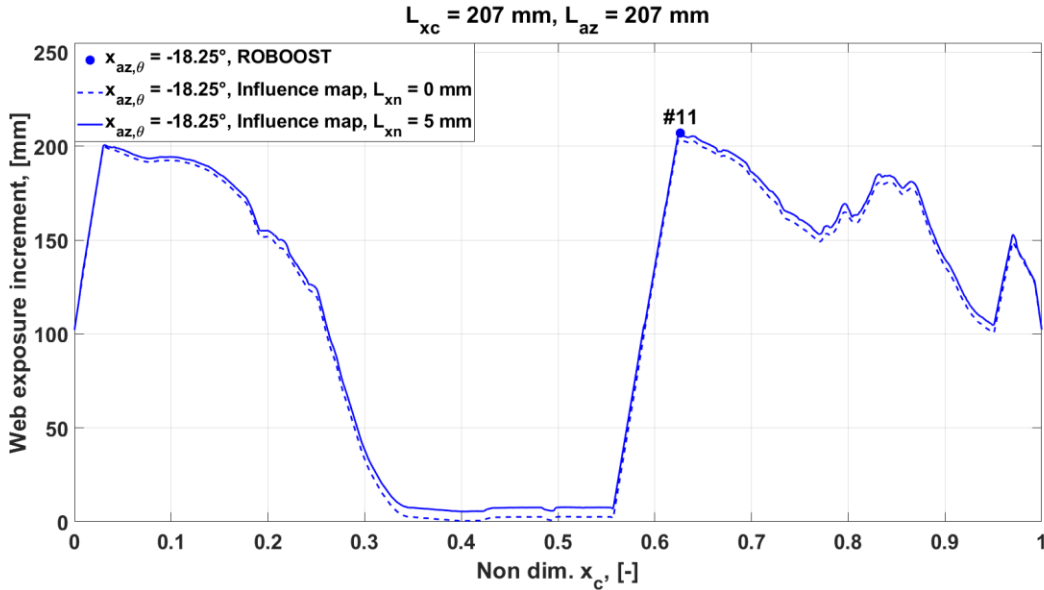


Figure 16: Comparison between ROBOOST result and debonding influence map with debonding
elongation along $e_{x_c}$ and $e_{az}$.

418
419
420    All results previously discussed were obtained with ROBOOST software installed on a calculator with the
421    following features: 16 Gb RAM, Intel Core i7-7th generation CPU machine with 3.10 GHz and NVIDIA
422    Quadro M1200 graphic card. ROBOOST simulations lasted 24 hours each, while exposure increase maps
423    lasted 1 hour each.

424 **4    Conclusions**

425    A novel procedure has been introduced to examine the effect of generic-shaped debondings on case-
426    insulating thermal protection material in terms of web exposure increment. By means of such method, the
427    most critical debonding positions on SRM case can be determined. Knowing the most critical exposure
428    regions can drive flaw inspection tests toward critical areas only, implying an optimized usage of x-ray
429    techniques. In the present work, debonding influence maps are evaluated on Z9 considering three sets of
430    debonding flaws, where the first one corresponds to debonding elongated along azimuthal direction, the
431    second one to debonding elongated along curvilinear coordinate direction and the last one to a debonding
432    extended of the same amount in both directions. Finally, those contour maps are validated by comparing
433    debonding web exposure increments with ROBOOST results obtaining a maximum percentage error of
434    1.8%, meaning that the method proposed can be considered satisfactory.

435    **Appendix A**

436    The abovementioned thermal protection exposure maps were obtained in a curvilinear reference frame
437    described in 0. This curvilinear coordinate system can be described by three orthogonal level surfaces:
438

439
$$\begin{cases} w_1 = f(x,y,z) \\ w_2 = g(x,y,z) \\ w_3 = z(x,y,z) \end{cases}$$

440

441    Where $w_1$, $w_2$ and $w_3$, are the curvilinear coordinate, $x, y, z$ are the cartesian coordinate. In the curvilinear
442    reference frame, the gradient is written as follows
443

444
$$\nabla \varphi = \sum_{j=1}^{3} \frac{1}{h_j} \frac{\partial \varphi}{\partial w_j} \hat{h}_j = \sum_{j=1}^{3} \frac{\vec{h}_j}{\left\| \vec{h}_j \right\|^2} \frac{\partial \varphi}{\partial w_j}$$

445
$$\vec{h}_j = \frac{\partial \vec{r}}{\partial w_j}$$

446
$$h_j = \left\| \frac{\partial \vec{r}}{\partial w_j} \right\|$$

447

448    Where $h_j$ are the Lamè coefficients, $\vec{r}$ is the position vector and in the cartesian coordinate it is written as
449    follows

450

$$\vec{r} = x\,e_x + y\,e_y + z\,e_z$$

452

Where $e_x, e_y, e_z$ are the cartesian basis. To evaluate the Lamè coefficients, the vector $\vec{r}$ needs to be written as function of the curvilinear coordinate $(w_1, w_2, w_3)$.

455

$$\vec{r} = k_x(w_1, w_2, w_3)\,e_x + k_y(w_1, w_2, w_3)\,e_y + k_z(w_1, w_2, w_3)\,e_z$$

457

$$\begin{cases} x = k_x(w_1, w_2, w_3) \\ y = k_y(w_1, w_2, w_3) \\ z = k_z(w_1, w_2, w_3) \end{cases}$$

459
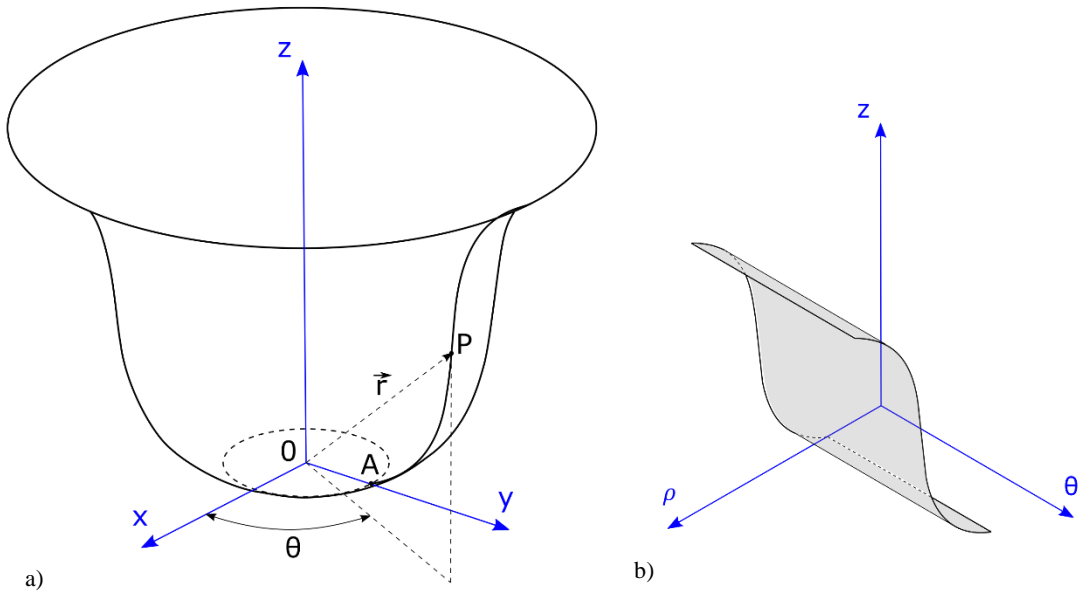


**Figure 17: Surface of revolution**

460
461

24
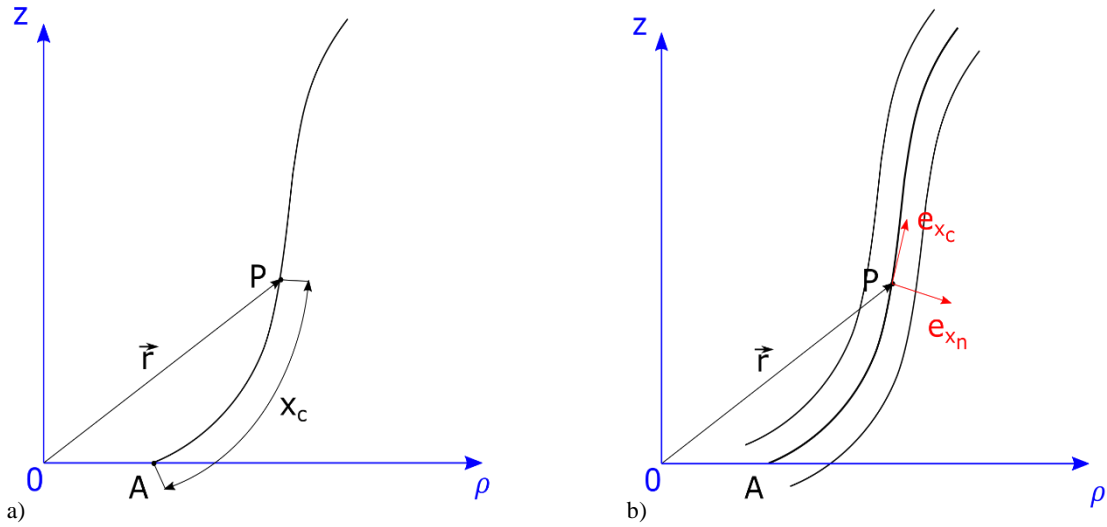
**Figure 18: Curvilinear coordinate system**

462

463

464    Figure 17a shows a general revolution surface obtained rotating the red curve along the $z$-axis. $w_2$ is defined

465    as the angle $\theta$ between the projection of $\vec{r}$ on $xy$-plane and the $x$-axis. Figure 17b shows the same surface

466    in cylindrical coordinate. Figure 18 shows the definition of $w_1$ and $w_3$: $w_1$ is defined as the length of red

467    curve from the point A to P, $w_3$ is the last coordinate defined by the basis always orthogonal to the case

468    surface.

469

$$w_1 = x_c = \int_A^P ds$$

470

$$w_2 = \theta$$

471

$$w_3 = x_n$$

472

473

474    Functions $k_x$, $k_y$ and $k_z$ in the general form are quite complicated to be obtained, but the gradient needs to

475    evaluate on the case surface, therefore $k_x$, $k_y$ and $k_z$ could be written considering small values of $x_n$. The

476    black solid curves in Figure 18b are the isoline for the curvilinear coordinate $x_n$. For small values of $x_n$, a

477    general point $(x, y, z)$ could be written as follows

$$\begin{cases} x = k_x(x_c, \theta, x_n) = \rho(x_c)\cos(\theta) + \hat{n}_x(x_c, \theta)x_n \\ y = k_y(x_c, \theta, x_n) = \rho(x_c)\sin(\theta) + \hat{n}_y(x_c, \theta)x_n \\ z = k_z(x_c, \theta, x_n) = a(x_c) + \hat{n}_z(x_c, \theta)x_n \end{cases}$$

478

479

480    Where $\hat{n}$ is the normal to the case. Therefore, it is straightforward the evaluation $\vec{r}$ and the Lamé

481    coefficients.

482

483    $$\vec{r} = [\,\rho(x_c)\cos(\theta) + \hat{n}_x(x_c,\theta)x_n\,]\,\hat{e}_1 + [\,\rho(x_c)\sin(\theta) + \hat{n}_y(x_c,\theta)x_n\,]\,\hat{e}_2$$

484    $$+ [\,a(x_c) + \hat{n}_z(x_c,\theta)x_n\,]\,\hat{e}_3$$

485    $$\vec{h}_1 = \frac{\partial \vec{r}}{\partial w_1} = \frac{\partial \vec{r}}{\partial x_c} = \left[\frac{\partial \rho}{\partial x_c}\cos(\theta) + \frac{\partial \hat{n}_x}{\partial x_c}x_n\right]e_x + \left[\frac{\partial \rho}{\partial x_c}\sin(\theta) + \frac{\partial \hat{n}_y}{\partial x_c}x_n\right]e_y + \left[\frac{\partial a}{\partial x_c} + \frac{\partial \hat{n}_z}{\partial x_c}x_n\right]e_z$$

486    $$\left\|\vec{h}_1\right\|^2 = \left(\frac{\partial \rho}{\partial x_c}\right)^2 + \left(\frac{\partial a}{\partial x_c}\right)^2 + \left[\left(\frac{\partial \hat{n}_x}{\partial x_c}\right)^2 + \left(\frac{\partial \hat{n}_y}{\partial x_c}\right)^2 + \left(\frac{\partial \hat{n}_z}{\partial x_c}\right)^2\right](x_n)^2 \;+\; 2\left[\frac{\partial \rho}{\partial x_c}\cos(\theta)\frac{\partial \hat{n}_x}{\partial x_c} + \frac{\partial \rho}{\partial x_c}\sin(\theta)\frac{\partial \hat{n}_y}{\partial x_c} + \right.$$

487    $$\left.\frac{\partial a}{\partial x_c}\frac{\partial \hat{n}_z}{\partial x_c}\right]x_n$$

488    $$\vec{h}_2 = \frac{\partial \vec{r}}{\partial w_2} = \frac{\partial \vec{r}}{\partial \theta} = \left[-\rho(x_c)\sin(\theta) + \frac{\partial \hat{n}_x}{\partial \theta}x_n\right]e_x + \left[\rho(x_c)\cos(\theta) + \frac{\partial \hat{n}_y}{\partial \theta}x_n\right]e_y + \left[\frac{\partial \hat{n}_z}{\partial \theta}x_n\right]e_z$$

489    $$\left\|\vec{h}_2\right\|^2 = \rho(x_c)^2 + \left[\left(\frac{\partial \hat{n}_x}{\partial \theta}\right)^2 + \left(\frac{\partial \hat{n}_y}{\partial \theta}\right)^2 + \left(\frac{\partial \hat{n}_z}{\partial \theta}\right)^2\right](x_n)^2 + 2\left[-\rho(x_c)\sin(\theta)\frac{\partial \hat{n}_x}{\partial \theta} + \rho(x_c)\cos(\theta)\frac{\partial \hat{n}_y}{\partial \theta}\right]x_n$$

490    $$\vec{h}_3 = \frac{\partial \vec{r}}{\partial w_3} = \frac{\partial \vec{r}}{\partial x_n} = \hat{n}_x(x_c,\theta)\,e_x + \hat{n}_y(x_c,\theta)\,e_y + \hat{n}_z(x_c,\theta)\,e_z$$

491    $$\left\|\vec{h}_3\right\|^2 = \hat{n}_x(x_c,\theta)^2 + \hat{n}_y(x_c,\theta)^2 + \hat{n}_z(x_c,\theta)^2 = 1$$

492

493    Imposing $x_n \to 0$ the Lamé coefficients becomes

494

495    $$\vec{h}_1 = \frac{\partial \vec{r}}{\partial w_1} = \frac{\partial \vec{r}}{\partial x_c} = \frac{\partial \rho}{\partial x_c}\cos(\theta)\,e_x + \frac{\partial \rho}{\partial x_c}\sin(\theta)\,e_y + \frac{\partial a}{\partial x_c}\,e_z$$

496    $$\left\|\vec{h}_1\right\|^2 = \left(\frac{\partial \rho}{\partial x_c}\right)^2 + \left(\frac{\partial a}{\partial x_c}\right)^2 \qquad\qquad (4)$$

497

498    $$\vec{h}_2 = \frac{\partial \vec{r}}{\partial w_2} = \frac{\partial \vec{r}}{\partial \theta} = -\rho(x_c)\sin(\theta)\,e_x + \rho(x_c)\cos(\theta)\,e_y$$

499    $$\left\|\vec{h}_2\right\|^2 = \rho(x_c)^2$$

500    $$\vec{h}_3 = \frac{\partial \vec{r}}{\partial w_3} = \frac{\partial \vec{r}}{\partial x_n} = \hat{n}_x(x_c,\theta)e_x + \hat{n}_y(x_c,\theta)e_y + \hat{n}_z(x_c,\theta)e_z = \hat{n}$$

501    $$\left\|\vec{h}_3\right\|^2 = 1$$

502
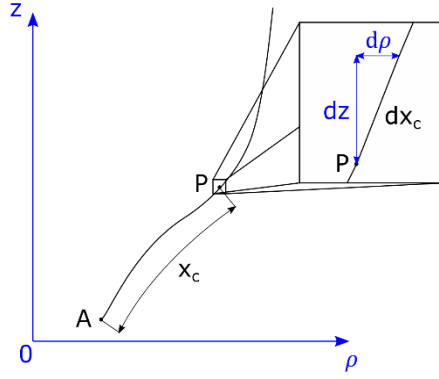
**Figure 19: geometric relation**

503

504

505   Using Figure 19, it possible to prove that $\left(\frac{\partial \rho}{\partial x_c}\right)^2 + \left(\frac{\partial a}{\partial x_c}\right)^2 = 1$.

506

507
$$d\rho = \frac{\partial \rho}{\partial x_c} dx_c, da = \frac{\partial a}{\partial x_c} dx_c$$

508

509   Applying the Pythagoras theorem on the triangle shown in Figure 19.

510

511
$$dx_c = \sqrt{d\rho^2 + da^2} = \sqrt{\left(\frac{\partial \rho}{\partial x_c}\right)^2 + \left(\frac{\partial a}{\partial x_c}\right)^2} \, dx_c$$

512   Therefore

513

514
$$\left(\frac{\partial \rho}{\partial x_c}\right)^2 + \left(\frac{\partial a}{\partial x_c}\right)^2 = 1$$

515

516   The previous results could be substituted into Eq. (4).

517
$$\nabla \varphi = \sum_{j=1}^{3} \frac{\vec{h}_j}{\|\vec{h}_j\|^2} \frac{\partial \varphi}{\partial w_j} = \frac{\partial \varphi}{\partial x_c} \frac{\vec{h}_1}{\|\vec{h}_1\|^2} + \frac{\partial \varphi}{\partial \theta} \frac{\vec{h}_2}{\|\vec{h}_2\|^2} + \frac{\partial \varphi}{\partial x_n} \frac{\vec{h}_3}{\|\vec{h}_3\|^2} =$$

518
$$= \frac{\partial \varphi}{\partial x_c} \left[ \frac{\partial \rho}{\partial x_c} \cos(\theta) \, e_x + \frac{\partial \rho}{\partial x_c} \sin(\theta) \, e_y + \frac{\partial a}{\partial x_c} \, e_z \right] + \frac{\partial \varphi}{\partial \theta} \frac{\left[ -\rho(x_c) \sin(\theta) \, e_x + \rho(x_c) \cos(\theta) \, e_y \right]}{\rho(x_c)^2}$$

519
$$+ \frac{\partial \varphi}{\partial x_n} \, \hat{n}$$

520
$$= \frac{\partial \varphi}{\partial x_c} \left[ \frac{\partial \rho}{\partial x_c} \cos(\theta) \, e_x + \frac{\partial \rho}{\partial x_c} \sin(\theta) \, e_y + \frac{\partial a}{\partial x_c} \, e_z \right] + \frac{\partial \varphi}{\partial \theta} \frac{1}{\rho(x_c)} \left[ -\sin(\theta) \, e_x + \cos(\theta) \, e_y \right] + \frac{\partial \varphi}{\partial x_n} \, \hat{n}$$

521

522
$$\hat{e}_{x_c} = \frac{\partial \rho}{\partial x_c} \cos(\theta) \, e_x + \frac{\partial \rho}{\partial x_c} \sin(\theta) \, e_y + \frac{\partial a}{\partial x_c} \, e_z$$

523
$$\hat{e}_\theta = -\sin(\theta) \, e_x + \cos(\theta) \, e_y$$

524
$$\nabla \varphi = \frac{\partial \varphi}{\partial x_c} \hat{e}_{x_c} + \frac{\partial \varphi}{\partial \theta} \frac{1}{\rho(x_c)} \hat{e}_\theta + \frac{\partial \varphi}{\partial x_n} \, \hat{n} \tag{5}$$

525

526

527   Finally, it is possible to introduce $x_{ac}$ coordinate: $x_{ac} = \theta \, \rho(x_c)$, therefore

528

529
$$\frac{\partial \varphi}{\partial \theta} = \frac{\partial \varphi}{\partial x_{ac}} \frac{\partial x_{ac}}{\partial \theta} = \frac{\partial \varphi}{\partial x_{ac}} \rho(x_c)$$

530

531   The Eq. 4 could be specialized for a discretized shape of the case. The parametric curve defined by

532   $(\rho(x_c), a(x_c))$ could be discretized in segments which could be described by the following law:

533

534
$$\alpha \rho + \beta z + \gamma = 0 \rightarrow z = -\frac{\alpha}{\beta} \rho \rightarrow dz = -\frac{\alpha}{\beta} d\rho$$

535   Where $\alpha$ and $\beta$ are the two coefficients obtained by the linearization.

536

537
$$x_c' = \int_C^D ds = \int_C^D \sqrt{(d\rho)^2 + dz^2} = \int_{\rho_C}^{\rho_D} \sqrt{1 + \left(\frac{\alpha}{\beta}\right)^2} \, d\rho = \sqrt{\frac{\beta^2 + \alpha^2}{\beta^2}} (\rho_D - \rho_C)$$

538
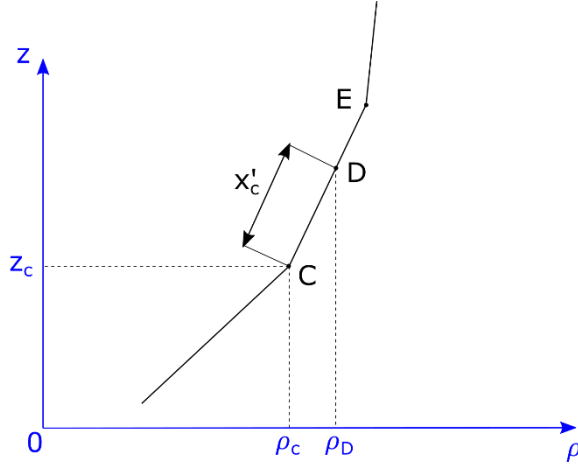
**Figure 20: Case profile discretization**

539

540

541
$$\rho_D = \frac{x_c'}{\sqrt{\frac{\beta^2 + \alpha^2}{\beta^2}}} + \rho_C = \sqrt{\frac{\beta^2}{\beta^2 + \alpha^2}} x_c' + \rho_C$$

542

543    This result could be substituted into the Eq. (5), where $\rho = \rho_D$:

544

545
$$\nabla\varphi = \frac{\partial\varphi}{\partial x_c}\hat{e}_{x_c} + \frac{\partial\varphi}{\partial\theta}\frac{1}{\sqrt{\frac{\beta^2}{\beta^2 + \alpha^2}}\,x_c' + \rho_C} + \frac{\partial\varphi}{\partial x_n}\hat{n}$$

546

547    Only the gradient component along $\hat{e}_{x_c}$ and $\hat{e}_\theta$ are important, because the thermal protection maps belong

548    to the case surface, therefore the previous gradient becomes

549

550
$$\nabla\varphi = \frac{\partial\varphi}{\partial x_c}\hat{e}_{x_c} + \frac{\partial\varphi}{\partial\theta}\frac{1}{\sqrt{\frac{\beta^2}{\beta^2 + \alpha^2}}\,x_c' + \rho_C}\,\hat{e}_\theta$$

551

552    **Nomenclature**

553    *Latin*

29

| 554 | $a(x_c)$ | = | case profile height function, $[m]$ |
|---|---|---|---|
| 555 | $ds$ | = | infinitesimal length, $[m]$ |
| 556 | $e_{az}$ | = | unit vector defining the orthonormal basis $(e_{x_c}, e_{az}, e_{x_n})$ |
| 557 | $e_x$ | = | unit vector defining the orthonormal basis $(e_x, e_y, e_z)$ |
| 558 | $e_{x_c}$ | = | unit vector defining the orthonormal basis $(e_{x_c}, e_{az}, e_{x_n})$ |
| 559 | $e_{x_n}$ | = | unit vector defining the orthonormal basis $(e_{x_c}, e_{az}, e_{x_n})$ |
| 560 | $e_y$ | = | unit vector defining the orthonormal basis $(e_x, e_y, e_z)$ |
| 561 | $e_z$ | = | unit vector defining the orthonormal basis $(e_x, e_y, e_z)$ and $(e_\rho, e_\vartheta, e_z)$ |
| 562 | $e_\vartheta$ | = | unit vector defining the orthonormal basis $(e_\rho, e_\vartheta, e_z)$ |
| 563 | $e_\rho$ | = | unit vector defining the orthonormal basis $(e_\rho, e_\vartheta, e_z)$ |
| 564 | $h_{az}$ | = | Lamè coefficient linked to the azimuthal coordinate $x_{az}$ |
| 565 | $h_j$ | = | Lamè coefficients |
| 566 | $h_{x_c}$ | = | Lamè coefficient linked to the azimuthal coordinate $x_c$ |
| 567 | $\hat{h}_j$ | = | unit vector regarding Lamè coefficients |
| 568 | $\vec{h}_j$ | = | vector regarding Lamè coefficients |
| 569 | $L_{az}$ | = | debonding size along $e_{az}$, $[m]$ |
| 570 | $L_{x_c}$ | = | debonding size along $e_{x_c}$, $[m]$ |
| 571 | $L_{x_n}$ | = | debonding size along $e_{x_n}$, $[m]$ |
| 572 | $\hat{n}$ | = | unit vector normal to the case surface |
| 573 | $\hat{n}_x$ | = | $x$-axis component of the unit vector normal to the case surface |
| 574 | $\hat{n}_y$ | = | $y$-axis component of the unit vector normal to the case surface |
| 575 | $\hat{n}_z$ | = | $z$-axis component of the unit vector normal to the case surface |
| 576 | $\vec{r}$ | = | position vector, $[m]$ |
| 577 | $w_1$ | = | general curvilinear coordinate |
| 578 | $w_2$ | = | general curvilinear coordinate |
| 579 | $w_3$ | = | general curvilinear coordinate |
| 580 | $x$ | = | coordinate of the orthonormal basis defined by $e_x$, $e_y$, and $e_z$ $[m]$ |
| 581 | $x_{az}$ | = | coordinate (expressed in length units) of the orthonormal basis defined by $e_{x_c}$, $e_{az}$, and $e_{x_n}$, |
| 582 | $[m]$ | | |
| 583 | $x_{az,\theta}$ | = | coordinate (expressed in angle units) of the orthonormal basis defined by $e_{x_c}$, $e_{az}$, and $e_{x_n}$, $[°]$ |
| 584 | $x_{az_{max}}$ | = | maximum exposure map extension along $e_{az}$, $[m]$ |

| 585 | $x_{az_{min}}$ | = | minimum exposure map extension along $e_{az}$, $[m]$ |
| --- | --- | --- | --- |
| 586 | $x_c$ | = | coordinate of the orthonormal basis defined by $e_{x_c}$, $e_{az}$, and $e_{x_n}$, $[m]$ |
| 587 | $x_{c_{max}}$ | = | maximum exposure map extension along $e_{x_c}$, $[m]$ |
| 588 | $x_{c_{min}}$ | = | minimum exposure map extension along $e_{x_c}$, $[m]$ |
| 589 | $x_{c_{0'}}$ | = | coordinate $x_c$ computed at local reference frame origin, namely 0', $[m]$ |
| 590 | $y$ | = | coordinate of the orthonormal basis defined by $e_x$, $e_y$, and $e_z$ $[m]$ |
| 591 | $z$ | = | coordinate of the orthonormal basis defined by $e_x$, $e_y$, and $e_z$ $[m]$ |

592 *Greek*

| 593 | $\alpha$ | = | coefficient of the line equation linked to the case envelope discretization |
| --- | --- | --- | --- |
| 594 | $\beta$ | = | coefficient of the line equation linked to the case envelope discretization |
| 595 | $\rho$ | = | coordinate of the orthonormal basis defined by $e_\rho$, $e_\vartheta$, and $e_z$ |
| 596 | $\rho_{0'}$ | = | radial position of the local reference frame origin expressed in global reference frame |
| 597 | | | cylindrical coordinates |
| 598 | $\rho(x_c)$ | = | case profile radius function |
| 599 | $\phi$ | = | exposure map regarding the case-insulating thermal protection material |
| 600 | $\varphi$ | = | generic scalar value |

601 *Acronyms*

| 602 | $CFD$ | = | Computational Fluid Dynamics |
| --- | --- | --- | --- |
| 603 | $ROBOOST$ | = | Rocket BOOst Simulation Tool |
| 604 | $SRM$ | = | Solid Rocket Motor |
| 605 | $ZEFIRO\ 9$ | = | ZEro First stage ROcket 9 |

606

610

611 **Declaration of competing interest**

612 The authors declare that they have no known competing financial interests or personal relationships that

613 could have appeared to influence the work reported in this paper.

614

615 **References**

616 [1]    G. Sutton, O. Biblarz, Rocket Propulsion Elements 9th Edition, Rocket Propuls. Elem. (2016).

617 [2]    F. Ponti, S. Mini, L. Fadigati, E. Corti, A. Annovazzi, Influence of Nozzle Radiation on Solid Rocket

618         Motors    Tail-off    Thrust,    Int.    J.    Energ.    Mater.    Chem.    Propuls.    (2021).

619         https://doi.org/10.1615/IntJEnergeticMaterialsChemProp.2021038491.

620 [3]    L.F.S. Hoffmann, F.C.P. Bizarria, J.W.P. Bizarria, Applied algorithm in the liner inspection of solid

621         rocket    motors,    Opt.    Lasers    Eng.    102    (2018)    143–153.

622         https://doi.org/10.1016/j.optlaseng.2017.11.006.

623 [4]    H.C. Yıldırım, Ş. Özüpek, Structural assessment of a solid propellant rocket motor: Effects of aging

624         and damage, Aerosp. Sci. Technol. 15 (2011) 635–641. https://doi.org/10.1016/j.ast.2011.01.002.

625 [5]    M.M. Iqbal, W. Liang, Modeling the moisture effects of solid ingredients on composite propellant

626         properties, Aerosp. Sci. Technol. 10 (2006) 695–699. https://doi.org/10.1016/j.ast.2006.07.003.

627 [6]    D. Dhital, J.R. Lee, C. Farrar, D. Mascarenas, A review of flaws and damage in space launch

628         vehicles:    Motors    and    engines,    J.    Intell.    Mater.    Syst.    Struct.    25    (2014)    524–540.

629         https://doi.org/10.1177/1045389X13493360.

630 [7]    D.L. Ban, B.D. Davidson, N.R. Moore, Probabilistic Failure Assessment with Application to Solid

631         Rocket Motors, Pasadena, California, 1990.

632 [8]    F. Ponti, S. Mini, A. Annovazzi, Numerical Evaluation of the Effects of Inclusions on Solid Rocket

633         Motor Performance, AIAA J. 58 (2020) 4028–4036. https://doi.org/10.2514/1.J058735.

634 [9]    S. WU, Y. LU, K. KUO, V. YANG, Anomalous combustion of solid propellant in a propagating

635         debond cavity, in: 30th Aerosp. Sci. Meet. Exhib., American Institute of Aeronautics and

636       Astronautics, Reston, Virigina, 1992. https://doi.org/10.2514/6.1992-770.

637    [10]    Hill Philip G., Peterson Carl R., Mechanics and thermodynamics of propulsion (2nd revised and

638       enlarged edition), 1992.

639    [11]    S. WU, Y. LU, K. KUO, V. YANG, Combustion-induced crack/debond propagation in a metalized

640       propellant, in: 28th Jt. Propuls. Conf. Exhib., American Institute of Aeronautics and Astronautics,

641       Reston, Virigina, 1992. https://doi.org/10.2514/6.1992-3506.

642    [12]    G.C. Sih, A model of debonding instability for solid propellant rocket motor: Part I — Uniform

643       longitudinal and transverse stress rate, Theor. Appl. Fract. Mech. 24 (1996) 93–113.

644       https://doi.org/10.1016/0167-8442(95)00034-8.

645    [13]    G.C. Sih, A model of debonding instability for solid propellant rocket motor: Part II — Unequal

646       longitudinal and transverse stress rate, Theor. Appl. Fract. Mech. 24 (1996) 115–134.

647       https://doi.org/10.1016/0167-8442(95)00035-6.

648    [14]    C. Hood, J. Sims, N. Knight, The Internal Flow Modeling of a Simulated Solid Propellant-Liner

649       Debond Using Loci-CHEM, in: 46th AIAA/ASME/SAE/ASEE Jt. Propuls. Conf. &amp; Exhib.,

650       American Institute of Aeronautics and Astronautics, Reston, Virigina, 2010.

651       https://doi.org/10.2514/6.2010-7164.

652    [15]    X. Guo, J.-T. Zhang, M. Zhang, L.-S. Liu, P.-C. Zhai, Q.-J. Zhang, Effects of liner properties on the

653       stress and strain along liner/propellant interface in solid rocket motor, Aerosp. Sci. Technol. 58

654       (2016) 594–600. https://doi.org/10.1016/j.ast.2016.09.020.

655    [16]    G. Zhou, X. Yin, Interfacial Fracture Toughness Between Hydroxyl-Terminated Polybutadiene

656       Solid Rocket Propellant and Liner, J. Propuls. Power. 34 (2018) 1305–1312.

657       https://doi.org/10.2514/1.B37019.

658    [17]    S. BEAN, Predicting X-rays for dynamic flaw detection in solid rockets, in: 27th Jt. Propuls. Conf.,

659       American Institute of Aeronautics and Astronautics, Reston, Virigina, 1991.

660       https://doi.org/10.2514/6.1991-3367.

33

661    [18]    B. Ghose, D.K. Kankane, Estimation of location of defects in propellant grain by X-ray radiography,

662            NDT E Int. 41 (2008) 125–128. https://doi.org/10.1016/j.ndteint.2007.08.005.

663    [19]    D. Gamdha, S. Unnikrishnakurup, K.J.J. Rose, M. Surekha, P. Purushothaman, B. Ghose, K.

664            Balasubramaniam, Automated Defect Recognition on X-ray Radiographs of Solid Propellant Using

665            Deep Learning Based on Convolutional Neural Networks, J. Nondestruct. Eval. 40 (2021) 18.

666            https://doi.org/10.1007/s10921-021-00750-4.

667    [20]    P. Lamarque, SRM improved X-rays examination: automatic detection in sight, Acta Astronaut. 54

668            (2004) 487–492. https://doi.org/10.1016/S0094-5765(03)00206-6.

669    [21]    G. Püskülcü, A. Ulas, 3-D grain burnback analysis of solid propellant rocket motors: Part 1 –

670            ballistic    motor    tests,    Aerosp.    Sci.    Technol.    12    (2008)    579–584.

671            https://doi.org/10.1016/j.ast.2008.02.001.

672    [22]    C. PATANCHON, Y. DENIGES, P. LAMARQUE, ARIANE 5 SOLID ROCKET MOTORS NON

673            DESTRUCTIVE TESTING, in: Non-Destructive Test. '92, Elsevier, 1992: pp. 176–180.

674            https://doi.org/10.1016/B978-0-444-89791-6.50041-X.

675    [23]    F. Ponti, N. Souhair, S. Mini, A. Annovazzi, 0D Unsteady - 1D Quasi-Stationary Internal Ballistic

676            coupling for ROBOOST simulation tool, in: AIAA Propuls. Energy 2019 Forum, American Institute

677            of Aeronautics and Astronautics, Reston, Virginia, 2019. https://doi.org/10.2514/6.2019-4140.

678    [24]    F. Ponti, S. Mini, A. Annovazzi, A simplified approach to predict Friedman Curl effect in a solid

679            rocket motor using ROBOOST simulation tool, in: AIAA Propuls. Energy 2019 Forum, American

680            Institute of Aeronautics and Astronautics, Reston, Virginia, 2019. https://doi.org/10.2514/6.2019-

681            3960.

682

683

684    **Vitae**

**Stefano Mini**, PhD in Mechanics and Advanced Engineering Sciences.
Research Fellow at the University of Bologna, Department of Industrial
Engineering. He received his master's degree in Aerospace Engineering with a
thesis regarding the design and implementation of a self-intersection removal
procedure for a solid rocket motor simulation program.

690    His research interest revolves around the modelling and design of simulators with
691    the aim of giving predictions about solid rocket motor performances. He is currently working on the
692    modelling of the thermal protection materials ablation phenomenon and their effect on the thrust final phase.
693

**Fabrizio Ponti** received his PhD in Machine Engineering from Polytechnic of Bari,
Italy, in 2001. He is currently Full Professor at University of Bologna since 2018,
teaching Aerospace Propulsion within the Master in Aerospace Engineering. His
main research interests are Solid Rocket Boosters simulation and modeling with
particular focus on 3D modeling of the burnback process, thermal protection ablation,
699    internal ballistics, and flaws modeling. He is also involved in other research topics
700    dealing with the modeling of the combustion process in internal combustion engines and gas turbines.
701

**Vittorio Ravaglioli**, PhD in Mechanics and Advanced Engineering Sciences.
Senior Assistant Professor at the University of Bologna, Department of Industrial
Engineering.
Academic Lecturer for the courses of Turbomachines (bachelor's in Aerospace
Engineering) and Internal Combustion Engines (International Master in
Advanced Automotive Engineering).
708    Personal research activities mainly focused on the development of models and innovative control strategies
709    for Advanced Propulsion Systems, both in Aerospace and Automotive field.
710

35

**Davide Moro** graduated in mechanical engineering at the University of Bologna (1988). He was researcher, associate and full professor (2001) at the same University, where, from November 2018 he is President of the School of Engineering.

His research activity is focused on gas turbine groups and internal combustion engines modeling and diagnosis. The main aim is the systematic analysis of specific work and efficiency improvement in order to choose the best system configuration, but he was also responsible of the development of diagnostic procedures and innovative combustion strategies, based on direct and indirect measurements.

**Adriano Annovazzi**, Senior Engineer at AVIO Space Propulsion Design Department. He was responsible for grain design and motor performance of military rocket missiles and Ariane 4/Ariane 5 solid boosters. Moreover, he focused on hybrid rocket motor design. Regarding the above-mentioned activities, he was involved as co-author in articles published in international journals.

At present, his activity revolves around numerical codes to give predictions concerning solid motor internal ballistics.